

# Delay analysis of ring resonator-based beam-forming network in z-domain

Md. Danish Nadeem<sup>1\*</sup>, Sanjeev Kumar Raghuwanshi<sup>1</sup>, Ritesh Kumar<sup>2</sup>

<sup>1</sup> Microwave Photonics Laboratory, Department of Electronics Engineering, Indian Institute of Technology (Indian School of Mines), Dhanbad Jharkhand-826004, India

<sup>2</sup> Shri Phaneshwar Nath Renu Engineering College, Araria, Bihar 854318, India

## Article info

### Article history:

Received 25 Dec. 2023

Received in revised form 21 Feb. 2024

Accepted 09 Mar. 2024

Available on-line 23 Apr. 2024

### Keywords:

Antenna element;  
beam-forming network;  
optical ring resonator.

## Abstract

During the next generation of wireless cellular networks, the millimeter-wave (mm-wave) spectrum will bring new opportunities for exceptionally high data transfer speeds and extensive network connectivity. Millimeter waves, on the other hand, are subject to a significant loss of propagation, which is the most significant impediment. A beneficial solution to this difficulty, which can be overcome, is to use a beam-forming system that consists of many antennas. The purpose of this study is to provide a concept for an integrated photonic beam-forming system that utilises multiple ring resonators for a  $1 \times 4$  phase array antenna operating in the Ka-Band frequency range. The waveguide technology is the foundation for a signal that operates at 28 GHz. It is through the use of the optical ring resonator that the actual time delay line may accomplish its goal. The suggested method can be implemented as a variable true time delay (TTD) line to change the radiation angle of phase array antennas (PAA). The main lobe radiated by the PAA can be directed squint-free between the angles from  $-28^\circ$  to  $+28^\circ$ . The mathematical analysis and design of the beam producing the structure are presented. Following that, delays of 650 ps, 350 ps, and 250 ps could be produced with coupling coefficients of  $\kappa = 0.5$ ,  $\kappa = 0.7$ , and  $\kappa = 0.9$ , respectively, and the associated phase shifts were  $0.469\pi$ ,  $0.146\pi$ , and  $0.387\pi$ .

## 1. Introduction

Microwave photonic technology in phase array antennas (PAA) is appealing due to its wide bandwidth operation, antenna remoting, immunity to electromagnetic interference, superior isolation, small size, and low weight [1, 2]. Microwave photonics may perform beam forming, frequency measurement, and signal filtering for phased arrays [3, 4]. Microwave phase shifting is essential for signal conditioning in 5G antenna remote units and military radar systems. Phase shifters require a large radio frequency (RF) range, fast response time, and fine-tuning resolution [5]. Beam forming with many antennas maximizes signal strength in one direction [6]. For high directional gain, many antennas are used in an array to focus the signal on the user, achieving satisfactory efficiency. Conventional electrical beam forming solutions using phase shifters as a delay generator are inefficient and

prone to a squinting impact on the beam. For this reason, the system is unable to perform properly at bands with higher frequencies [7, 8] because, as the frequency varies, the beam moves further away from the direction of the target. The network connecting the elements to the transmitter or receiver strongly affects PAA performance. The main job of a beam-forming network (BFN) is to set the right delays to send the signal in the right direction. Beam forming using optical technologies can solve the aforementioned concerns. Many optical beam-forming researchers use the concept of true time delay (TTD). Several optical TTD beam-forming designs have been reported [9, 10]. A simplified form of a TTD-based optical beam-forming system is shown in Fig. 1. For practical considerations in 5G communication networks, smaller devices are required. Realisation of a TTD unit via optical fibre is not sufficient for this purpose. Photonic integration technologies with low attenuation, low weight, tiny size, and independence from frequency can help create a complex beamformer [11].

\*Corresponding author at: [danish.iitism@gmail.com](mailto:danish.iitism@gmail.com)

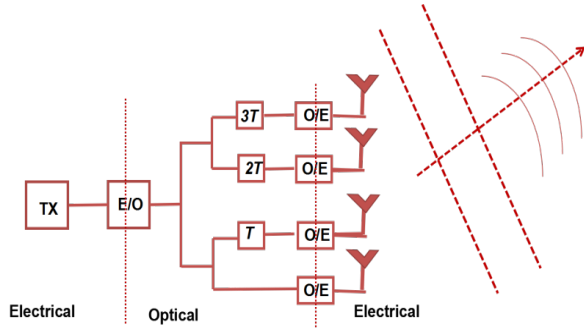


Fig. 1. Optical beam-forming system.

Switching delay lines [12], photonic crystal fibre [13], and fibre Bragg grating [14] have all been used in the successful realisation of integrated delay line topologies. An optical all-pass ring resonator has a tiny footprint and can constantly tune the delay. In this work, the authors provide a detailed description of an optical ring resonator (ORR)-based  $1 \times 4$  photonic beamformer that uses silicon-on-insulator (SOI) waveguide technology. An mm-wave frequency of 28 GHz is selected because of its low atmospheric effect. Due to its lesser propagation loss and coupling loss with an optical fibre, a SOI rib waveguide is used to construct the photonic beamformer components. One of the guiding layers is made of silicon with a high refractive index ( $n_{Si} = 3.473$  at 1550 nm), and it is bordered by silicon dioxide with a low refractive index ( $n_{SiO_2} = 1.444$ ). For a TTD line design, the effective refractive index ( $n_{eff}$ ) and group index ( $n_g$ ) of the waveguide must be addressed. Maxwell's equations were solved using a completely vectorial finite-difference mode solver to get single-mode waveguide dimensions. The effective refractive index and group index,  $n_{eff}$  and  $n_g$  at 1550 nm are 2.5 and 5, respectively.

## 2. Theory

In Fig. 2, the authors present a schematic layout of the proposed optical beam-forming network (OBFN) for a  $1 \times 4$  linear phased array antenna, an mm-wave signal modulates the laser source continuous light wave in the Mach-Zehnder modulator (MZM), and modulated light from the MZM is connected to a  $1 \times 4$  photonic beam-forming network made up of a  $1 \times 4$  splitter and an all-pass ring resonator. The passive  $1 \times 4$  optical splitter waveguide device splits the modulated light into four different configurations of ring resonators. In the second step, the split signal is sent through a single, double, triple, or quadruple series cascaded ring resonator time delay element to introduce a delay that can be adjusted to achieve a broad range of beam steering. The RF port of MZM receives an RF signal with a frequency of  $\omega_{RF}$  and amplitude  $V_e$ , because of this, the modulated signal with a  $\lambda_i$  carrier wavelength is produced by MZM and can be written as [15]

$$E_{out(MZM),i} = \sqrt{P_i} e^{j\left(\omega_i t + \frac{\pi V_e}{V_\pi} \cos(\omega_{RF} t)\right)}, \quad (1)$$

where  $V_\pi$  is the MZM half-wave voltage and  $P_i$  is the optical power at the corresponding  $\omega_i$  frequency of the optical carrier signal. The wavelength  $\lambda_i$  of the carrier is

linked to the angular frequency  $\omega_i$ . An MZM modulated output is approximated as [16]

$$E_{out(MZM),i}(t) = \sqrt{P_i} \left[ J_0(\beta) e^{j\omega_i t} + J_1(\beta) e^{j(\omega_i t + \omega_{RF} t)} - J_1(\beta) e^{j(\omega_i t - \omega_{RF} t)} \right]. \quad (2)$$

MZM modulation index is  $\beta = \frac{\pi V_e}{V_\pi}$ . Due to the lower value of the phase modulation index, higher-order harmonics are ignored in (2), which yields an equation comparable to the double-sided (DSB)-modulated signal.

The electric field at each port of the  $1 \times 4$  splitter is represented as [17]

$$E_{out,m}(t) = \frac{E_{out(MZM),i}(t) 10^{-\alpha_s/20}}{\sqrt{4}} = \frac{E_{out(MZM),i}(t) 10^{-\alpha_s/20}}{2}, \quad (3)$$

where  $m = 1, 2, 3, 4$  (an  $n^{\text{th}}$  arm of splitter),  $E_{out,m}(t)$  are the electric fields induced at the output of the  $1 \times 4$  splitter, respectively,  $\alpha_s$  is the waveguide propagation loss in dB/cm. In this work, the waveguide propagation loss  $\alpha_s$  is employed to adjust the ORR to the low-loss scenario. The computed waveguide propagation loss in dB/cm uses the given relation

$$\alpha_s = 20 \log(e^\alpha) = 20\alpha \cdot \log(e) = 8.686\alpha,$$

where  $\alpha$  is the amplitude attenuation constant. The electric field that is produced at the output of the beamformer is then transmitted to the photodiode (PD) after it has been transmitted through a waveguide with a length of  $L_w$ . The electric field induced at each PD is given by

$$E_{PDm_{in}}(t) = E_{out,m}(t) (-j\beta L_w) \exp\left(\frac{-\alpha L_w}{2}\right) H_p(f), \quad (4)$$

where  $H_p(f)$  is the transfer function of the different configurations of ring resonators and  $p$  is the number of rings connected in a cascaded form. Similarly, the induced electric field of the beamformer through ring and waveguide is fed to the photodiodes (PDs) PD1, PD2, PD3, PD4 after propagating through a different configuration of a cascaded ring resonator of each port of the PDs which are given by below relation

$$\begin{aligned} E_{PDm_{in}}(t) &= E_{out,m}(t) (-j\beta L_{wm}) \exp\left(\frac{-\alpha L_{wm}}{2}\right) H_p(f) \\ &= \frac{E_{out(MZM),i} 10^{\frac{-\alpha_s}{20}}}{2} (-j\beta L_{wm}) \exp\left(\frac{-\alpha L_{wm}}{2}\right) H_p(f). \end{aligned} \quad (5)$$

Substituting  $E_{out}(t)$  value in (5), the authors obtain:

$$\begin{aligned} E_{PDm_{in}}(t) &= \frac{\sqrt{P_i} \left[ J_0(\beta) e^{j\omega_i t} + J_1(\beta) e^{j(\omega_i t + \omega_{RF} t)} - J_1(\beta) e^{j(\omega_i t - \omega_{RF} t)} \right] 10^{\frac{-\alpha_s}{20}}}{2} \\ &\quad \cdot (-j\beta L_{wm}) \exp\left(\frac{-\alpha L_{wm}}{2}\right) H_p(f), \end{aligned} \quad (6)$$

where  $H_p(f)$  are the transfer functions of different configurations of the ring with rectangular waveguides and  $L_{wm}$  is the corresponding length of the waveguide.

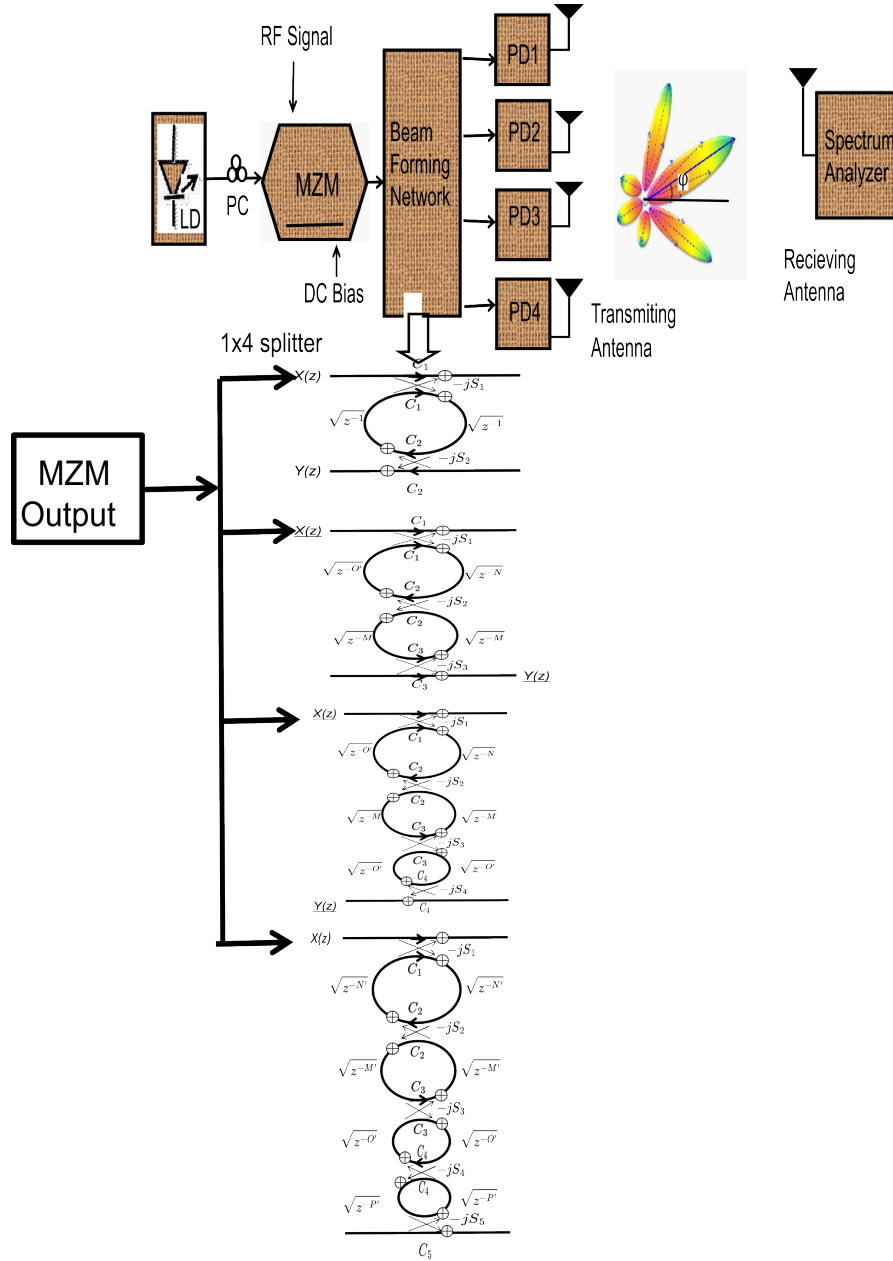


**Fig. 2.** Schematic layout of the proposed beam-forming system.

The signal from the beam-forming network is fed to PD1, PD2, PD3, and PD4 to provide an RF signal of different power. Table 1 shows modelling with derivation of a single and series multiple cascaded ring resonator using Mason's gain rule. These cascading ring structures are working as a beam-forming network. PD output provides a photonic RF signal, which has different magnitudes and phases or delays which will ensure the antenna excitation and radiation pattern in the far field. This magnitude and phases depend on the transfer function of the ring resonator or series cascaded ring resonators. And the transmittance of the given structure mainly depends on phase ( $\varphi$ ) and

coupling coefficient ( $\kappa$ ), the photocurrent in the PDs is represented as

$$I_{PDm_{out}}(t) = R_{PD} |E_{PDm_{in}}(t)|^2 + I_{PDm_N}(t), \quad (7)$$

where  $I_{PDm_{out}}(t)$  is the photocurrent as measured at the corresponding PD output,  $R_{PD}$  is the responsivity of PDs.  $I_{PDm_N}(t)$  reflects the contribution to the noise current made by several different causes, including shot noise and dark current noise in PDs so the equation of PD current at the output of PD is

$$I_{PDm_{out}}(t) = R_{PD} \left| \frac{\sqrt{P_i} [J_0(\beta) e^{j\omega_i t} + J_1(\beta) e^{j(\omega_i t + \omega_{RF} t)} - J_1(\beta) e^{j(\omega_i t - \omega_{RF} t)}] 10^{-\alpha_s/20}}{2} (-j\beta L_{wm}) \exp\left(\frac{-\alpha L_{wm}}{2}\right) H_p(f) \right|^2 + I_{PDm_N}(t). \quad (8)$$

It is clear from the aforementioned equations that the photocurrent at the PD output is affected by several factors, including the coupling coefficient, waveguide loss, round-trip path length, and phase shift of the all-pass ring resonator.

As per the proposed beam-forming system as shown in Fig. 2, the incoming signal will be linked into the first ring at the MZM output with a coupling coefficient of  $\kappa$ , as the remaining very less amount of signal propagates through the straight waveguide to the through-port that is not sufficient to excite the PD. With the same coupling coefficient  $\kappa$ , the portion of the signal that travels in the ring will be linked once again into the waveguide beneath the ring. These phenomena provide some delay signal concerning the reception without a ring at the PD output. For all the rings, this propagation operation continues. There will be a series cascaded combination of one, two, three, and four rings that will interact with the straight waveguides bus of each unit. The rings that are at the top and bottom of the cascade will be the rings that interact with the waveguides bus that leads to the through-port and drop-port, respectively. The interaction between the rings in this configuration is direct and takes the form of propagation between rings themselves. All tests will be conducted with a coupling coefficient of 0.5, 0.7, and 0.9 and ring lengths are 14.42  $\mu\text{m}$ , 16.48  $\mu\text{m}$ , 19.57  $\mu\text{m}$ , and 29  $\mu\text{m}$ . Effective refractive index  $n_{\text{eff}} = 2.5$ , group index  $n_g = 5$  simulating the effects of cascading exclusively.

### 3. Modelling of ring resonator for time delay analysis in z-domain

Light is an electromagnetic wave, but it is a time variable, as well as a space variable. Moslehi [18] has experimentally shown that when light waves travel through a waveguide, then their delay can be represented as a conventional transfer function of delay. The transfer function of delay can be represented in the Laplace domain, as well as the z-domain. The most fundamental element useful to represent Bragg grating could be a partially reflected mirror which is equivalent to the well-known Fabry-Perot (FP) cavity. In a typical all-pass configuration, as shown in Fig. 3(a), the Z-transform schematic of the single ring resonator is represented in Fig. 3(b), a straight waveguide is positioned next to a ring near a couple that allows light to pass in and out of the resonator via an evanescent field. The input complex mode amplitude,  $E_i$ , and the output complex mode amplitude,  $E_t$ , are the normalised measurements of the complex modes in the straight waveguide. Both  $t$  and  $\kappa$  represent waveguide fields through the coupling coefficient and the cross-over coupling coefficient, respectively. Such that  $t^2 + \kappa^2 = 1$ . The interaction between light and the attenuation constant in the ring resonator filter is shown in Fig. 3(b) and can be characterised by the matrix relation as in (9). Here, it can be considered  $C_1 = C_2 = C$  and  $S_1 = S_2 = S$ .

$$\begin{bmatrix} E_{t1} \\ E_{t2} \end{bmatrix} = a \begin{bmatrix} C & jS \\ -jS^* & C^* \end{bmatrix} \begin{bmatrix} E_{i1} \\ E_{i2} \end{bmatrix}. \quad (9)$$

Coupler inputs are denoted by  $E_{i1}$  and  $E_{i2}$  whereas coupler outputs are denoted by  $E_{t1}$  and  $E_{t2}$ , and the amplitude

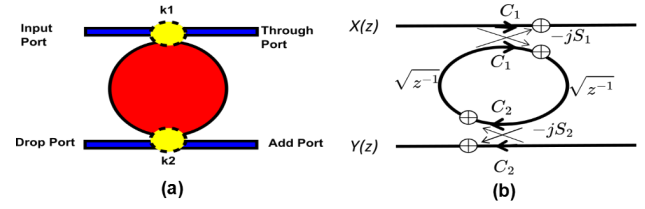


Fig. 3. (a) Schematic of the all-pass ring resonator configuration used as a delay element. (b) Z-transform diagram followed by a signal flow graph (SFG) representation of the single ring resonator using a directional optical coupler.

transmission coefficient of the coupler is denoted by  $a$ . The representation of the through-port transmission is denoted by the equation  $C = \sqrt{1 - \kappa}$ , while the designation of the cross-port transmission would be  $-jS = -j\sqrt{\kappa}$ , the coupling ratio  $\kappa$  should be wavelength-independent; the effective group index is constant and does not vary from its nominal value. The transfer function of a ring resonator can be calculated using the Mason's gain formula [19, 20]. The ring round-trip loss can be expressed as  $\alpha_s = \exp(\alpha L)$  [21], where  $\alpha$  is the average ring loss per unit length and  $L$  is the circumference of the ring. One is chosen as the amplitude transmission coefficient. The total transmittance of a single ring with a single waveguide is defined as

$$H(f) = \frac{S_1 S_2 \sqrt{\alpha_s z^{-1}}}{1 - C_1 C_2 \alpha_s z^{-1}}, \quad (10)$$

where  $z^{-1}$  is generally known as the unit delay in the z-domain and the entire ring perimeter represents the unit delay length for a single ring resonator;  $z^{-1} = e^{-(\alpha + j\beta)L}$  and assuming the loss is not considered here;  $\alpha$  is the amplitude attenuation constant and  $\beta$  is the propagation constant given by  $\beta = \frac{2\pi n_{\text{eff}}}{\lambda}$ ;  $L$  is the circumference of the resonator. Assuming that there is no propagation loss in the resonator, i.e., all power coming to the input port reaches the output port. Then  $\alpha$  will be zero and the magnitude of the transfer function will be 1. Similarly, Table 1 shows the structural representation and transmittance with derivation using Mason's gain rule of the single, double, triple, and quad-ring resonator. The idea of group delay is used to demonstrate the delay characteristics of the ORR. The transfer function  $H(f)$  of any signal using signal flow graph (SFG) as per the Meson's gain rule is given by

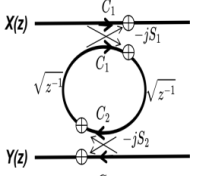
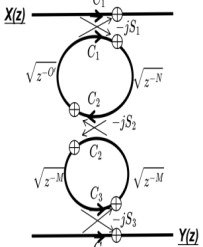
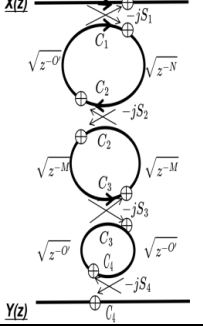
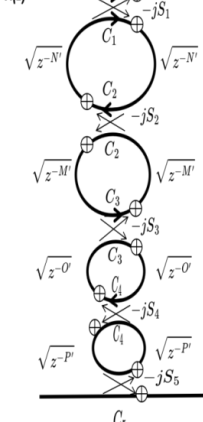
$$H(f) = \frac{\sum T_n \Delta_n}{\Delta}. \quad (11)$$

In the above equation,  $T_n$  represents the transmittance of the  $n^{\text{th}}$  forward path, and  $\Delta$  represents the determinant of the graph

$$\Delta = 1 - \sum L_1 + \sum L_2 + \sum L_3 + \dots$$

In this context,  $\sum L_1$  denotes the total transmittance of all specific graphs of single closed paths (loops),  $\sum L_2$  denotes the total transmittance of all potential permutations of two non-touching closed paths,  $\sum L_3$  denotes the total

**Table 1.** Mason's gain formula-based transfer function of cascaded ring resonator

Structure name	Structure	Forward path	Individual loop	Two non-touching loops	Three non-touching loops	Transfer function
Single ring		$T = -S_1 S_2 \sqrt{Z^{-1}}$	$L_1 = C_1 C_2 \sqrt{Z^{-1}}$			$T_f = \frac{S_1 S_2 \sqrt{Z^{-1}}}{1 - C_1 C_2 \sqrt{Z^{-1}}}$
Double ring		$T = -jS_1 S_2 S_3 \cdot \sqrt{Z^{-(N+M)}}$	$L_1 = C_1 C_2 \sqrt{Z^{-N}}$ $L_2 = C_2 C_3 \sqrt{Z^{-M}}$ $L_3 = C_1 C_3 S_2^2 \sqrt{Z^{-(N+M)}}$	$L_3 = C_1 C_3 C_2^2 \sqrt{Z^{-(N+M)}}$		$T_f = \frac{jS_1 S_2 S_3 \sqrt{Z^{-(N+M)}}}{1 - (C_1 C_2 \sqrt{Z^{-N}} + C_2 C_3 \sqrt{Z^{-M}} + C_1 C_3 S_2^2 \sqrt{Z^{-(N+M)}})}$
Triple ring		$T = -jS_1 S_2 S_3 S_4 \cdot \sqrt{Z^{-(N'+M'+O')}}$	$L_1 = C_1 C_2 \sqrt{Z^{-N}}$ $L_2 = C_2 C_3 \sqrt{Z^{-M'}}$ $L_3 = C_3 C_4 \sqrt{Z^{-O'}}$ $L_4 = -C_1 C_3 S_2^2 \sqrt{Z^{-(N'+M')}}$ $L_5 = -C_2 C_4 S_3^2 \sqrt{Z^{-(M'+O')}}$ $L_6 = -C_1 C_4 S_2^2 S_3^2 \cdot \sqrt{Z^{-(N'+M'+O')}}$	$L_1 = -C_1 C_3 C_2^2 \sqrt{Z^{-(N'+M')}}$ $L_2 = C_2 C_4 C_3^2 \sqrt{Z^{-(M'+O')}}$ $L_3 = C_1 C_2 C_3 C_4 \sqrt{Z^{-(N'+O')}}$ $L_4 = -C_1 C_4 C_3^2 S_2^2 \sqrt{Z^{-(N'+M'+O')}}$ $L_5 = -C_1 C_4 C_2^2 S_3^2 \sqrt{Z^{-(N'+M'+O')}}$	$L_5 = -C_1 C_4 C_2^2 C_3^2 \sqrt{Z^{-(N'+M'+O')}}$	$T_f = \frac{-jS_1 S_2 S_3 S_4 \sqrt{Z^{-(N'+M'+O')}}}{1 - C_1 C_2 \sqrt{Z^{-N'}} - C_2 C_3 \sqrt{Z^{-M'}} - C_3 C_4 \sqrt{Z^{-O'}} + C_1 C_3 \sqrt{Z^{-(N'+M')}} + C_2 C_4 \sqrt{Z^{-(M'+O')}} - C_1 C_4 \sqrt{Z^{-(N'+M'+O')}} + C_1 C_2 C_3 C_4 \sqrt{Z^{-(N'+O')}}}$
Quad-ring		$T = -jS_1 S_2 S_3 S_4 S_5 \cdot \sqrt{Z^{-(N+M+O+P)}}$	$l_1 = C_1 C_2 Z^{-N}$ $l_2 = C_2 C_3 Z^{-M}$ $l_3 = C_3 C_4 Z^{-O}$ $l_4 = C_4 C_5 Z^{-P}$ $l_5 = -C_1 C_3 S_2^2 Z^{-(N+M)}$ $l_6 = -C_2 C_4 S_3^2 Z^{-(M+O)}$ $l_7 = -C_3 C_5 S_4^2 Z^{-(O+P)}$ $l_8 = C_1 C_4 S_2^2 S_3^2 Z^{-(N+M+O)}$ $l_9 = -C_2 C_5 S_3^2 S_4^2 Z^{-(M+O+P)}$ $l_{10} = -C_1 C_5 S_2^2 S_3^2 S_4^2 \cdot Z^{-(N+M+O+P)}$	$l_{12} = C_1 C_3 C_2^2 Z^{-(N+M)}$ $l_{23} = C_2 C_4 C_3^2 Z^{-(M+O)}$ $l_{34} = C_3 C_5 C_4^2 Z^{-(O+P)}$ $l_{31} = C_1 C_2 C_4^2 Z^{-(N+O)}$ $l_{41} = C_1 C_2 C_4 C_5 Z^{-(N+P)}$ $l_{42} = C_2 C_3 C_4 C_5 Z^{-(M+P)}$ $l_{54} = -C_1 C_3 C_4 C_5 S_2^2 Z^{-(N+M+P)}$ $l_{53} = -C_1 C_4 C_3^2 C_5 S_2^2 Z^{-(N+M+O)}$ $l_{61} = -C_1 C_4 C_2^2 S_3^2 Z^{-(N+M+O)}$ $l_{64} = -C_2 C_5 C_4^2 S_3^2 Z^{-(M+O+P)}$ $l_{71} = -C_1 C_3 C_2 C_5 S_4^2 Z^{-(N+O+P)}$ $l_{72} = -C_2 C_5 C_3^2 S_4^2 Z^{-(M+O+P)}$ $l_{75} = -C_1 C_5 C_3^2 S_2^2 Z^{-(N+M+O+P)}$ $l_{84} = -C_1 C_5 C_4^2 S_2^2 S_4^2 Z^{-(N+M+O+P)}$ $l_{91} = -C_1 C_5 C_2^2 S_3^2 S_4^2 Z^{-(N+M+O+P)}$	$l_{123} = -C_1 C_2^2 C_3^2 C_4 Z^{-(N+M+O)}$ $l_{234} = -C_2 C_4^2 C_3^2 C_5 Z^{-(M+O+P)}$ $l_{124} = C_1 C_2^2 C_3 C_4 C_5 Z^{-(N+M+P)}$ $l_{134} = C_1 C_2 C_3 C_5 Z^{-(N+M+O)}$ $l_{614} = -C_1 C_5 C_2^2 C_4^2 S_3^2 \cdot Z^{-(N+M+O+P)}$ $l_{712} = -C_1 C_5 C_2^2 C_3^2 S_4^2 \cdot Z^{-(N+M+O+P)}$ $l_{534} = -C_1 C_5 C_4^2 C_3^2 S_2^2 \cdot Z^{-(N+M+O+P)}$	$T_f = \frac{j\sqrt{k_1 k_2 k_3 k_4 k_5} \sqrt{Z^{-(N+M+O+P)}}}{1 - C_1 C_2 Z^{-N} - C_2 C_3 Z^{-M} + C_3 C_4 Z^{-O} + C_4 C_5 Z^{-P} - C_1 C_3 Z^{-(N+M)} + C_2 C_4 Z^{-(M+O)} + C_3 C_5 Z^{-(O+P)} - C_1 C_4 Z^{-(N+M+O)} - C_2 C_5 Z^{-(M+O+P)} + C_1 C_2 C_3 C_4 Z^{-(N+O)} + C_1 C_2 C_4 C_5 Z^{-(N+P)} + C_2 C_3 C_4 C_5 Z^{-(M+P)} - C_1 C_3 C_4 C_5 Z^{-(N+M+P)} - C_1 C_3 C_2 C_5 Z^{-(N+O+P)} C_1 C_5 Z^{-(N+M+O+P)}}$



transmittance of all potential permutations of three non-touching loops, and so on. It is important to note that  $\Delta n$  represents the value of  $\Delta$  for the portion of the graph that does not touch the  $n^{\text{th}}$  forward path. Table 1 presented below delineates the derivation of transfer functions for single, double, triple, and quad-ring resonators in tabular format.

Phase of  $H(f)$  is

$$\phi = \tan^{-1} \left( \frac{\text{Re}\{H(f)\}}{\text{Im}\{H(f)\}} \right)$$

and group delay is defined as [22]

$$\tau_{GD}(f) = -\frac{d\phi}{d\omega}. \quad (12)$$

After simplification, the frequency-dependent group delay of one ring and one waveguide can be expressed using the following mathematical expression

$$\tau_{GD}(f) = \frac{\kappa \tau_r}{(2 - \kappa - 2\sqrt{1 - \kappa \cos(2\pi f \tau_r + \phi)})}, \quad (13)$$

where  $\tau_r = \frac{n_{eff}L}{c}$ . Figures 4 and 5 show the transmittance spectrum and group delay spectrum of single, double, triple, and quad-ring resonator configuration, respectively. The derivation of all four structures of cascaded ring resonator are discuss in Table 1.

From the transmittance graph, the free spectral range (FSR) value for finding the delay generated by each configuration of the ring resonator can be calculated. As in (8), it is clear that the coupling coefficients of the all-pass ring resonator affect the photocurrent at the PD output. In Fig. 6, the group delay plot shows the variation of coupling coefficient for three different values, at  $\kappa = 0.5$ ,  $\kappa = 0.7$ , and  $\kappa = 0.9$ , respectively. When an ORR is used as an optical delay element, this feature is the most important one. For the proposed ORR to meet the low-loss condition, it is assumed that the round-trip loss  $\alpha_s$  is less than 1 dB. The frequency response of an ORR is controlled by the coupling ratio and the additional round-trip phase shift, which determine the offset of the resonance frequency. When  $\kappa = 0$ , nothing at all of the incoming light connects to the ring, the ORR produces no phase shifts or delays. In the case when  $\kappa$  equals 1, the light that is introduced connects entirely to the ring, and then completely disconnects after a single round-trip. In this particular scenario, the ORR performs the same function as a waveguide with dimensions of  $2 \times 2$ , so the coupling coefficient  $\kappa$  should lie in the range of  $0 < \kappa < 1$ .

After one FSR, the phase transition is  $2\pi$ . However, if the value of  $\kappa$  is lower than the critical coupling point, a negative group delay will occur in the area of the resonance frequency for a lossy ORR [23]. From Fig. 6, the coupling of coefficient of  $\kappa = 0.5$ ,  $\kappa = 0.7$ , and  $\kappa = 0.9$  is taken to find the group delay response. By selecting the appropriate phase  $\phi$  and the coupling coefficient  $\kappa$  of every individual ORR in the in-series cascaded structure, a smooth delay band with a wide bandwidth will be obtained as shown in Fig. 7. It is evident that the delay band formed a ripple and is not perfectly smooth; the ripple will cause different frequency components of the signals that fall within the

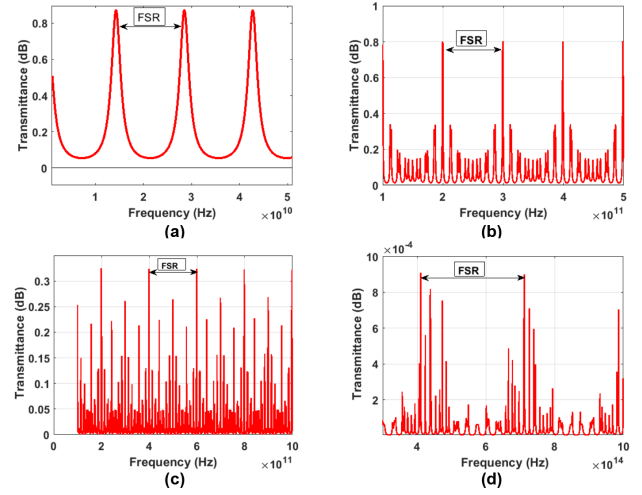


Fig. 4. Transmittance spectrum of (a) single, (b) double, (c) triple, and (d) quad-ring resonator configuration.

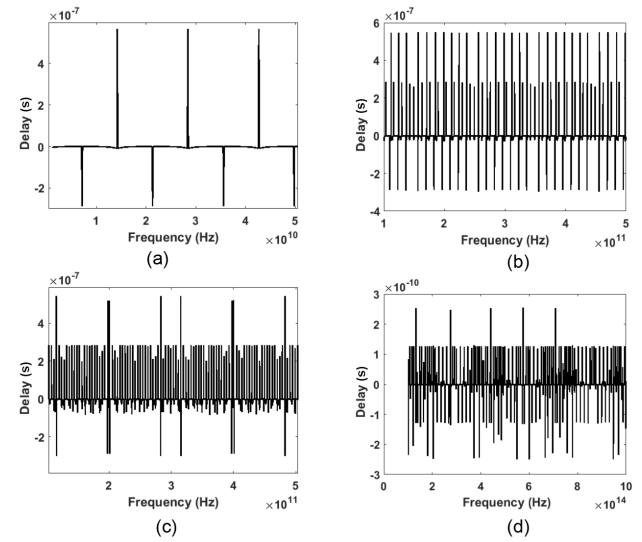


Fig. 5. Simulated group delay response of (a) single, (b) double, (c) triple, and (d) quad-ring resonator configuration.

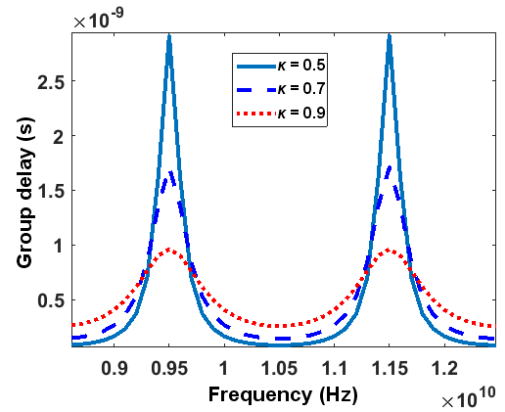


Fig. 6. Group delay response of ring resonator for the different coupling coefficient.

delay band to experience unequal delays as a result. These ripples cause changes in the antenna beam angle when ORRs are used in an OBFN as the delay elements [24, 25].

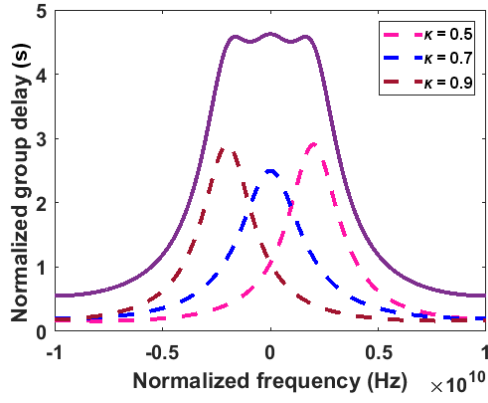


Fig.7. Three ORRs in a cascade group delay response and their corresponding individual ORRs.

#### 4. Beam-forming system based on multiple ORR structures

By introducing the round-trip phase shift  $\varphi$  of the ring resonator, the group delay response in (12) is derived by putting  $\tau_r = \frac{n_g L}{c}$  as the round-trip propagation time where the speed of light is denoted by the letter  $c$ . The group delay responses for beam-forming network using coupling coefficients of  $\kappa = 0.5$ ,  $\kappa = 0.7$ , and  $\kappa = 0.9$  in the ring resonator for single, double, triple, and quadruple structures are shown in Fig. 8. The simulated and theoretical group delay achieved between the waveguides of the TTD lines of the proposed beam-forming system are shown in Table 2, respectively. Thus, the time delay achieved by the proposed beam-forming system for  $\kappa = 0.5$ ,  $\kappa = 0.7$ , and  $\kappa = 0.9$   $\Delta\tau_0 = 650$  ps,  $\Delta\tau_0 = 350$  ps, and  $\Delta\tau_0 = 250$  ps.

According to the theory of true-time delay-based beam-forming system, the relation between the expected beam angle  $\theta_0$  and the necessary inter-element phase difference  $\Delta\phi_0$  is as follows:

$$\Delta\phi_0 = kd\sin\theta_0, \quad (14)$$

where  $k = 2\pi/\lambda_{RF}$ ,  $\lambda_{RF}$  is the wavelength of a signal in free space denoted by  $\lambda_{RF}$ , and the distance between antenna elements is denoted by  $d$ . Using the formula provided, with a constant inter-element spacing linear array antenna, the desired beam angle in the far-field radiation

pattern can be generated by defining the incremental time delay that must be maintained between adjacent waveguides of an optical TTD unit. This will allow the antenna to produce the desired beam angle

$$\Delta\tau_0 = \frac{kd\sin\theta_0}{2\pi f_{RF}}. \quad (15)$$

To prevent the formation of grating lobes, it is recommended that the spacing  $d$  between adjacent elements be equal to  $\lambda_{RF}/2$ . After making the substitutions  $k = 2\pi/\lambda_{RF}$  and  $\lambda_{RF}/2$ , the above equation becomes

$$\Delta\tau_0 = \frac{\sin\theta_0}{2f_{RF}} \quad (16)$$

$$\theta_0 = \sin^{-1}(2f_{RF}\Delta\tau_0). \quad (17)$$

based on the incremental time delay  $\Delta\tau_0$  transmission of the signal. Equation (17) demonstrates that the antenna radiates in a particular direction  $\theta_0$ .

#### 5. Simulated results and analysis for beam-forming steering

In this study, the authors use the idea of a group delay to describe the properties of the delay that the modulated RF signal encounters. The group delay is defined as the inverse of the phase response of the transfer function in an ORR as a function of the angular frequency  $\omega$ . Here, there is a formula for a group delay that takes into account the frequency component [26, 27]

$$\tau_{GD} = -\frac{d\varphi(\omega)}{d\omega}. \quad (18)$$

The frequency-dependent incremental group delay can be expressed in (18). Table 2 shows the theoretical and achievable different delays for the different cascaded structures of the beam-forming system. Figure 9 shows the polar plot of the beam-forming radiation pattern of different frequencies from 28–34 GHz. From Table 2, the authors found that the theoretical value of the beam angle has a good resemblance with the simulation one, in some cases, both theoretical and simulated results overlapped

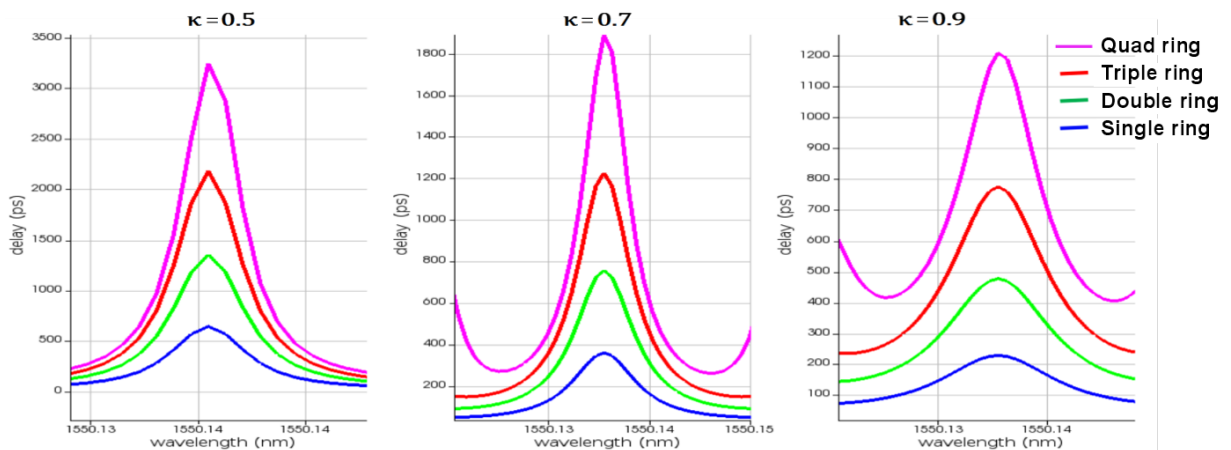
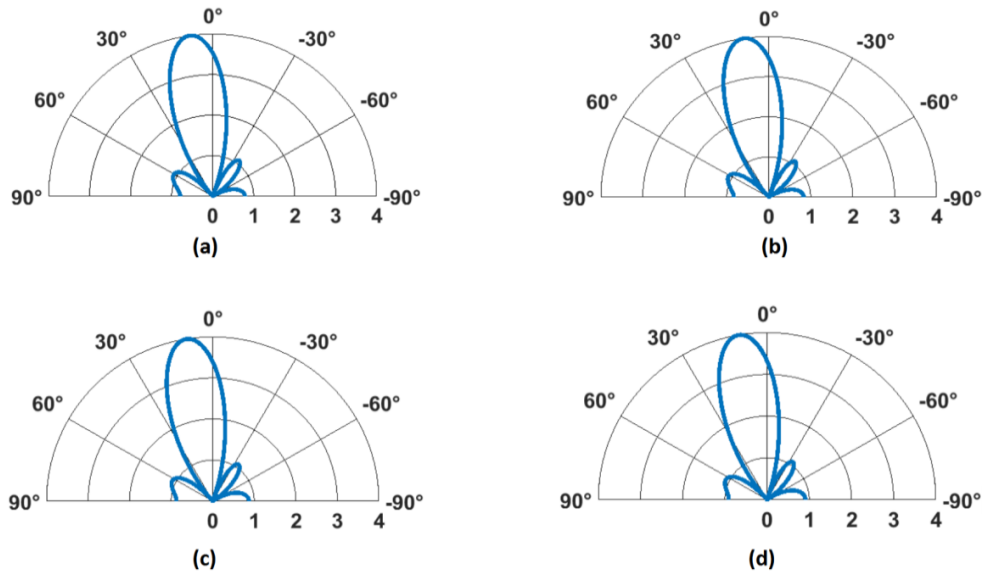


Fig.8. Simulated group delay response of the proposed beam-forming network for all structures (single, double, triple and quad-ring resonator) for different values: (a)  $\kappa = 0.5$ , (b)  $\kappa = 0.7$ , (c)  $\kappa = 0.9$ .

**Table 2.**  
Group delay response of all cascaded configurations of the ring resonator.

Operative frequency $f_{RF}$	Delay (ps) $\tau_{GD}$	Delay (ps) $\Delta\tau_0 = \tau_{GDn} - \tau_{GDn-1}$	Beam angle (theoretical) $\theta_0 = \sin(f_{RF}\Delta\tau_0)$	Beam angle (simulated)
28 GHz	250	250	$8.0^\circ$	$7.65^\circ$
30 GHz	500	250	$8.62^\circ$	$8.16^\circ$
32 GHz	750	250	$9.20^\circ$	$9.07^\circ$
34 GHz	1000	250	$9.78^\circ$	$9.56^\circ$



**Fig. 9.** The radiation pattern of different RF frequencies: (a) 28 GHz, (b) 30 GHz, (c) 32 GHz, (d) 34 GHz.

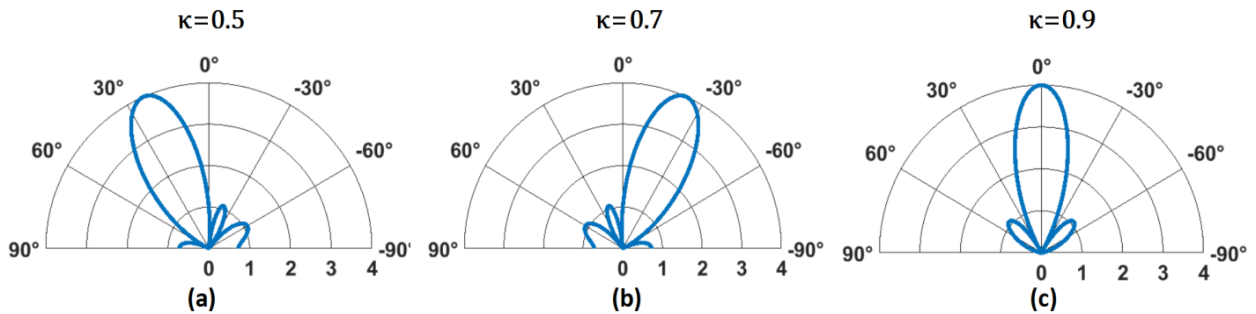


**Fig.10.** The radiation pattern for different coupling coefficients at 28 GHz: (a)  $\kappa = 0.5$ , (b)  $\kappa = 0.7$ , (c)  $\kappa = 0.9$ .

and could not be distinguish in these plots. Table 1 has been followed to obtain Fig. 9, which shows the actual beam-forming response in the polar plot of each unit of the beam-forming network at a frequency of 28–34 GHz. Delay of the proposed different cascaded architecture of ring resonator as a delay element which corresponds to a beam directing angle of  $-28^\circ$ ,  $+28^\circ$ ,  $0^\circ$  for coupling coefficient of  $\kappa = 0.5$ ,  $\kappa = 0.7$ , and  $\kappa = 0.9$ , respectively. Tables 3, 4, and 5 show the theoretical and simulated beam angle for different coupling coefficients at 28 GHz. Figure 10 depicts beam-forming angles at 28 GHz of  $-28^\circ$ ,  $+28^\circ$ , and  $0^\circ$  for the coupling coefficient of  $\kappa = 0.5$ ,  $\kappa = 0.7$ , and  $\kappa = 0.9$ , respectively. According to the literature, as the

number of antennas remains constant, the back-lobe power increases as the scan angle grows larger. Power is emitted in an unacceptable direction. More antennas can be employed to suppress back lobes and boost main lobe output. This study uses a group delay to illustrate the modulated RF signal temporal delay. Figure 11 demonstrates the relationship between steering angle and time delay for different mm-wave frequencies. A 250 ps delay was achieved between the TTD lines of the beamformer using a single, double, triple, and quadruple cascaded structure of ring resonator. The phase difference value was  $0.387\pi$ , and the steering angle ranged from  $-28^\circ$  to  $+28^\circ$  at an mm-wave frequency of 28 GHz.



**Table 3.**Theoretical and simulated beam angle for coupling coefficient of  $\kappa = 0.5$  at 28GHz

Operative frequency $f_{RF}$ (GHz)	Coupling coefficient ( $\kappa$ )	Delay element structure	Group delay ( $\tau_{GD}$ ) (ps)	Delay (ps)		Beam angle (theoretical)	Beam angle (simulated)
				$\Delta\tau_0 = \tau_{GDn} - \tau_{GDn-1}$	$\theta_0 = \sin(f_{RF}\Delta\tau_0)$		
28	0.5	Single ring	650	650		+28.0°	+26.65°
		Double ring	1300				
		Triple ring	1950				
		Quad ring	2600				

**Table 4.**Theoretical and simulated beam angle for coupling coefficient of  $\kappa = 0.7$  at 28 GHz.

Operative frequency $f_{RF}$ (GHz)	Coupling coefficient ( $\kappa$ )	Delay element structure	Group delay ( $\tau_{GD}$ ) (ps)	Delay (ps)		Beam angle (theoretical)	Beam angle (simulated)
				$\Delta\tau_0 = \tau_{GDn} - \tau_{GDn-1}$	$\theta_0 = \sin(f_{RF}\Delta\tau_0)$		
28	0.7	Single ring	350	350		0°	0.25°
		Double ring	700				
		Triple ring	1050				
		Quad ring	1450				

**Table 5.**Theoretical and simulated beam angle for coupling coefficient of  $\kappa = 0.9$  at 28 GHz.

Operative frequency $f_{RF}$ (GHz)	Coupling coefficient ( $\kappa$ )	Delay element structure	Group delay ( $\tau_{GD}$ ) (ps)	Delay (ps)		Beam angle (theoretical)	Beam angle (simulated)
				$\Delta\tau_0 = \tau_{GDn} - \tau_{GDn-1}$	$\theta_0 = \sin(f_{RF}\Delta\tau_0)$		
28	0.9	Single ring	250	250		-28.0°	-26.65°
		Double ring	500				
		Triple ring	750				
		Quad ring	1000				

## 6. Conclusions

In this paper, the authors present a proposal for a ring resonator-based photonic beam-forming network for 28–34 GHz transmissions, i.e., based on waveguide technology. It is necessary to make use of the micro-ring resonator to successfully construct the actual time delay line. The design of ring resonators with radii of 14.42  $\mu\text{m}$ , 16.48  $\mu\text{m}$ , 19.57  $\mu\text{m}$ , and 29  $\mu\text{m}$ , respectively, is currently being computed using waveguide technology. The next step is to outline the beam-forming structure design, after which the mathematical analysis will be presented. The group delay might be set to 650 ps, 350 ps, or 250 ps for coupling coefficient of  $\kappa = 0.5$ ,  $\kappa = 0.7$ , and  $\kappa = 0.9$ , respectively, and corresponding phase shifts are  $0.469\pi$ ,  $0.146\pi$ ,  $0.387\pi$ , respectively.

## Acknowledgements

This work is carried out from the research grant under the grant no.: ERIP/ER/202206004/M/01/1805 (Sanction Code of ER&IPR: DGT/M/ERIP/GIA/22-23/115/008 dated 08/08/2022) provided by Defence Research and Development Organization (DRDO), Government of India

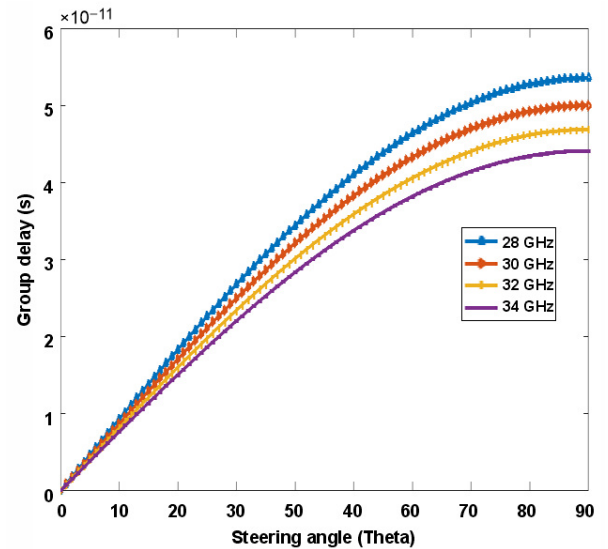


**Fig. 11.** The relationship between time delay and steering angle for various mm-wave frequencies.

(GOI) under Extramural Research funding scheme with the project entitled “Design and Development of Frequency Stable and High Q-Factor Optoelectronic Oscillator Assisted by Microwave Photonic Techniques”.

## References

- [1] Minasian, R. A. Ultra-wideband and adaptive photonic signal processing of microwave signals. *IEEE J. Quantum Electron.* **52**, 1–13 (2016). <https://doi.org/10.1109/JQE.2015.2499729>
- [2] Minasian, R. A., Chan, E. H. W. & Yi, X. Microwave photonic signal processing. *Opt. Express* **21**, 22918–22936 (2013). <https://doi.org/10.1364/OE.21.022918>
- [3] Yi, X., Chew, S. X., Song, S., Nguyen, L. & Minasian, R. A. Integrated microwave photonics for wideband signal processing. *Photonics* **4**, 46 (2017). <https://doi.org/10.3390/photonics4040046>
- [4] Minasian, R. A. Photonic signal processing of microwave signals. *IEEE Trans. Microw. Theory Tech.* **54**, 832–846 (2006). <https://doi.org/10.1109/TMTT.2005.863060>
- [5] Nguyen, T. A., Chan, E. H. W. & Minasian, R. A. Instantaneous high-resolution multiple-frequency measurement system based on frequency-to-time mapping technique. *Opt. Lett.* **39**, 2419–2422 (2014). <https://doi.org/10.1364/OL39002419>
- [6] Sadhu, B. *et al.* A 28 GHz 32-Element Phased-Array Transceiver IC with Concurrent Dual Polarized Beams and 1.4 Degree Beam-Steering Resolution for 5G Communication. in *2017 IEEE International Solid-State Circuits Conference (ISSCC)* 3373–3391 (IEEE, 2017). <https://doi.org/10.1109/ISSC.2017.2766211>
- [7] Nadeem, M. D. & Raghuvanshi, S. K. Optimised design & analysis of high gain 3×3 square patch array antennas with six ports for airborne application in S-band. *J. Electromagn. Waves Appl.* **36**, 2419–2434 (2022). <https://doi.org/10.1080/09205071.2022.2080592>
- [8] Aluigi, L., Orecchini, G. & Larcher, L. A 28 GHz Scalable Beamforming System for 5G Automotive Connectivity: An Integrated Patch Antenna and Power Amplifier Solution. in *2018 IEEE MTT-S International Microwave Workshop Series on 5G Hardware and System Technologies (IMWS-5G)* 1–3 (IEEE, 2018). <https://doi.org/10.1109/IMWS-5G.2018.8484325>
- [9] Akiyama, T., Ando, T. & Hirano, Y. Fourier Transform Optically Controlled Phased Array Antenna. in *2013 18th OptoElectronics and Communications Conference held jointly with 2013 International Conference on Photonics in Switching WO4\_4* (OSA, 2013). [https://doi.org/10.1364/OECC\\_PS.2013.WO4\\_4](https://doi.org/10.1364/OECC_PS.2013.WO4_4)
- [10] Ortega, B., Mora, J. & Chulia, R. Optical beamformer for 2-D phased array antenna with subarray partitioning capability. *IEEE Photon. J.* **8**, 1–9 (2016). <https://doi.org/10.1109/JPHOT.2016.2550323>
- [11] Li, Y., Ghafoor, S., Satyanarayana, K., El-Hajjar, M. & Hanzo, L. Analogue wireless beamforming exploiting the fiber-nonlinearity of radio over fiber-based C-RANs. *IEEE Trans. Veh. Technol.* **68**, 2802–2813 (2019). <https://doi.org/10.1109/TVT.2019.2893589>
- [12] Jung, B. M. & Yao, J. A two-dimensional optical true time-delay beamformer consisting of a fiber Bragg grating prism and switch-based fiber-optic delay lines. *IEEE Photon. Technol. Lett.* **21**, 627–629 (2009). <https://doi.org/10.1109/LPT.2009.2015275>
- [13] Sancho, J. *et al.* Integrable microwave filter based on a photonic crystal delay line. *Nat. Commun.* **3**, 1075 (2012). <https://doi.org/10.1038/ncomms2092>
- [14] Kumar, S. N. & Raghuvanshi, S. K. Demonstration of Highly Steerable Beamforming System Incorporating a Waveguide of Spatially Distributed Fiber Bragg Grating. in *2019 6th International Conference on Signal Processing and Integrated Networks (SPIN)* 367–370 (IEEE, 2019). <https://doi.org/10.1109/SPIN.2019.8711766>
- [15] Kumar, R., Raghuvanshi, S. K. & Nadeem, D. Chirped fiber grating and specialty fiber based multiwavelength optical beamforming network for 1X8 phased array antenna in S-band. *Optik* **243**, 167044 (2021). <https://doi.org/10.1016/j.ijleo.2021.167044>
- [16] Kumar, R. & Raghuvanshi, S. K. photonic generation of multiple shapes and sextupled microwave signal based on polarization modulator. *IEEE Trans. Microw. Theory Tech.* **69**, 3875–3882 (2021). <https://doi.org/10.1109/TMTT.2021.3076996>
- [17] Kumari, S. & Prince, S. Photonic beamforming incorporating ring resonator based on silicon-on-insulator waveguide technology. *Silicon* **14**, 8869–8879 (2022). <https://doi.org/10.1007/s12633-022-01684-w>
- [18] Moslehi, B., Goodman, J. W., Tur, M. & Shaw, H. J. Fiber-optic lattice signal processing. *Proc. IEEE* **72**, 909–930 (1984). <https://doi.org/10.1109/PROC.1984.12948>
- [19] Rabus, D. G. *Ring Resonators: Theory and Modeling. Integrated Ring Resonators.* (Springer Berlin Heidelberg, 2007).
- [20] Kumar, R., Singh, Y., Raghuvanshi, S. K., Chandra, S. & Nadeem, D. Delay and Dispersion Investigation of Optical Components for Microwave Photonic Filter. in *VLSI, Microwave and Wireless Technologies. Lecture Notes in Electrical Engineering* (eds. Mishra, B. & Tiwari, M.) vol. **877** (Springer, 2023). [https://doi.org/10.1007/978-981-19-0312-0\\_69](https://doi.org/10.1007/978-981-19-0312-0_69)
- [21] Kumari, S. & Prince, S. Photonic integrated cmos-compatible true time delay based broadband beamformer. *Opt. Quant. Electron.* **55**, 1198 (2023). <https://doi.org/10.1007/s11082-023-05492-3>
- [22] Roeloffzen, C. G. H. *et al.* Integrated photonic beamformer employing continuously tunable ring resonator-based delays in CMOS-compatible LPCVD waveguide technology. *Proc. SPIE* **7135**, 71341K (2008). <https://doi.org/10.1117/12.803719>
- [23] Nadeem, D. *et al.* Design and analysis of photonic beam forming system using ring resonator for 1 × 4 phase array antenna in Ka-Band. *Proc. SPIE* **12429**, 124290S (2023). <https://doi.org/10.1117/12.2648280>
- [24] Nadeem, D. *et al.* Modeling of quad ring resonator for tunable delay line in z-domain analysis. *Proc. SPIE* **12429**, 114290N (2023). <https://doi.org/10.1117/12.2648319>
- [25] Nadeem, M. D., Raghuvanshi, S. K. & Kumar, R. Efficient photonics beam forming system incorporating super structure fiber Bragg grating for application in Ku band. *Opt. Fiber Technol.* **80**, 103436 (2023). <https://doi.org/10.1016/j.yofte.2023.103436>
- [26] Nadeem, D., Kumar, R., Raghuvanshi, S. K. & Kumar, S. Advanced photonic-assisted antenna array: efficient beam steering system for radar application. *Proc. SPIE* **12890**, 128900J-1 (2024). <https://doi.org/10.1117/12.2691273>
- [27] Danish, N., Sanjeev, K. R. & Yadav, R. K. Recent advancement on photonic feeding antennas for microwave beam steering. *I-Manager's J. Commun. Eng. Systems (JCS)* **8**, 10 (2019). <https://doi.org/10.26634/jcs.8.1.15888>